

On the use of helium-filled soap bubbles for large-scale tomographic PIV in wind tunnel experiments

*Original*

On the use of helium-filled soap bubbles for large-scale tomographic PIV in wind tunnel experiments / Scarano, F.; Ghaemi, S.; Caridi, G. C. A.; Bosbach, J.; Dierksheide, U.; Sciacchitano, A.. - In: EXPERIMENTS IN FLUIDS. - ISSN 0723-4864. - 56:2(2015). [10.1007/s00348-015-1909-7]

*Availability:*

This version is available at: 11583/2835613 since: 2020-06-14T15:14:03Z

*Publisher:*

Springer Verlag

*Published*

DOI:10.1007/s00348-015-1909-7

*Terms of use:*

This article is made available under terms and conditions as specified in the corresponding bibliographic description in the repository

*Publisher copyright*

(Article begins on next page)

# On the use of helium-filled soap bubbles for large-scale tomographic PIV in wind tunnel experiments

Fulvio Scarano · Sina Ghaemi · Giuseppe Carlo Alp Caridi ·  
Johannes Bosbach · Uwe Dierksheide ·  
Andrea Sciacchitano

Received: 10 November 2014 / Revised: 20 January 2015 / Accepted: 22 January 2015 / Published online: 11 February 2015  
© The Author(s) 2015. This article is published with open access at Springerlink.com

**Abstract** The flow-tracing fidelity of sub-millimetre diameter helium-filled soap bubbles (HFSB) for low-speed aerodynamics is studied. The main interest of using HFSB in relation to micron-size droplets is the large amount of scattered light, enabling larger-scale three-dimensional experiments by tomographic PIV. The assessment of aerodynamic behaviour closely follows the method proposed in the early work of Kerho and Bragg (Exp Fluids 50:929–948, 1994) who evaluated the tracer trajectories around the stagnation region at the leading edge of an airfoil. The conclusions of the latter investigation differ from the present work, which concludes sub-millimetre HFSB do represent a valid alternative for quantitative velocimetry in wind tunnel aerodynamic experiments. The flow stagnating ahead of a circular cylinder of 25 mm diameter is considered at speeds up to 30 m/s. The tracers are injected in the free-stream and high-speed PIV, and PTV are used to obtain the velocity field distribution. A qualitative assessment based on streamlines is followed by acceleration and slip velocity measurements using PIV experiments with fog droplets as a term of reference. The

tracing fidelity is controlled by the flow rates of helium, liquid soap and air in HFSB production. A characteristic time response, defined as the ratio of slip velocity and the fluid acceleration, is obtained. The feasibility of performing time-resolved tomographic PIV measurements over large volumes in aerodynamic wind tunnels is also studied. The flow past a 5-cm-diameter cylinder is measured over a volume of  $20 \times 20 \times 12 \text{ cm}^3$  at a rate of 2 kHz. The achieved seeding density of  $<0.01 \text{ ppp}$  enables resolving the Kármán vortices, whereas turbulent sub-structures cannot be captured.

## 1 Introduction

Aerodynamic studies performed by means of tunnel experiments are increasingly requiring particle image velocimetry (PIV) to characterize the velocity field, streamlines topology, unsteady effects and turbulence. A survey of applications is given in Raffel et al. (2007), where the planar PIV technique is used for wind tunnel investigations. The appearance of tomographic PIV (Elsinga et al. 2006) has moved further the research tools for investigating the fundamental aspects of complex turbulent flows (Westerbeek et al. 2013). Despite its rapid development, tomographic PIV has not been used within industrial wind tunnels, mostly due to the limited extent of the measurement domain achieved so far.

In the past two decades, PIV in wind tunnels has evolved from experiments done at moderate scale, typically  $10 \times 10 \text{ cm}^2$ , up to large scales of  $50 \times 50 \text{ cm}^2$  both for aeronautical and automotive applications (Kompenhans et al. 2000; Beaudoin and Aider 2008). Literature abounds of experiments with measurement domain exceeding a square metre, but this is mostly done by patching several

---

F. Scarano · G. C. A. Caridi (✉) · A. Sciacchitano  
Aerospace Engineering Department, Delft University  
of Technology, Delft, The Netherlands  
e-mail: g.caridi@tudelft.nl

S. Ghaemi  
Mechanical Engineering Department, University of Alberta,  
Edmonton, AB, Canada

J. Bosbach  
Institute of Aerodynamics and Flow Technology,  
German Aerospace Center (DLR), Göttingen, Germany

U. Dierksheide  
LaVision GmbH, Göttingen, Germany

fields of view of typically  $40 \times 30 \text{ cm}^2$  (Carmer et al. 2008; Lignarolo et al. 2014 among others).

When moving to three-dimensional measurements in air flows, tomographic PIV has been applied in several wind tunnel experiments. A recent review (Scarano 2013) discusses the evolution of several parameters, including the measurement volume. The initial tomo-PIV experiment of Elsinga et al. (2006) was conducted over a volume of  $13 \text{ cm}^3$ . Later tomo-PIV experiments in air conducted by Schröder et al. (2009), Humble et al. (2009), Violato et al. (2011) and Ghaemi and Scarano (2011) were also performed on a volume not exceeding  $20 \text{ cm}^3$ . Slightly larger measurement volumes have been obtained by Schröder et al. (2011) and Atkinson et al. (2011), which did not exceed  $52 \text{ cm}^3$ . To date, the largest investigated volume has been reported by Fukuchi (2012) who measured over  $16 \times 22 \times 8 \text{ cm}^3$ , although results with an acceptable reconstruction signal-to-noise ratio were obtained up to a volume depth of 5 cm.

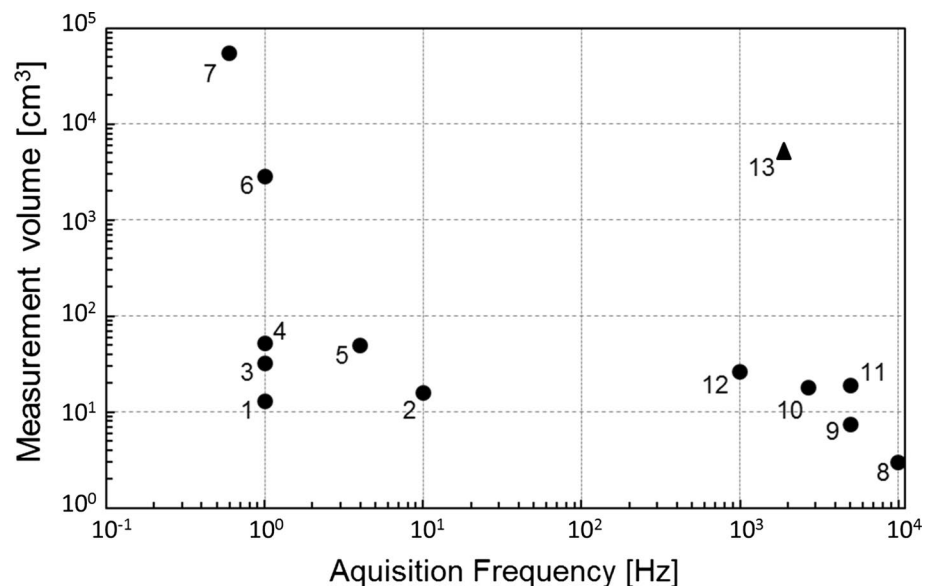
The main factors limiting the upscale of PIV to macroscopic dimensions are the limited pulse energy from the illumination source, the scattering efficiency of the tracers and the sensitivity and spatial resolution of the imagers. The progress obtained in the last 20 years is largely due to the evolution of sensor technology that has led to CCD/CMOS cameras up to 30 Mpixel and with quantum efficiency around 50 % (Adrian 2005). Comparatively, the pulse energy of PIV lasers has essentially remained the same during these years. The same can be said for the seeding tracers for air flows, which are still based on fog generators or Laskin nozzles for large-scale wind tunnels (Raffel et al. 2007).

The imaging of the tracer particles in a tomographic PIV experiment is conducted at illumination intensity

typically an order of magnitude smaller than that of planar PIV due to the expansion of the laser beam over a large cross section. The problem is further exacerbated by the small optical aperture (high f-number) of the imaging system, needed to ensure focused particles across the whole measurement depth. As a result, the peak intensity of particle images decreases by almost an order of magnitude when the volume depth is doubled. As a consequence, the intensity counts of particle images rarely exceed a few hundreds. This problem has been addressed for conventional tomo-PIV experiments by applying high-power lasers or multi-pass light amplification system (Ghaemi and Scarano 2010), which enables the use of tomographic PIV for high-speed measurements in air flows at moderate speed (Schröder et al. 2008; Ghaemi and Scarano 2011; Pröbsting et al. 2013). A survey of relevant experiments conducted in airflows is given in Fig. 1, where the measurement volume is plotted against the acquisition frequency. One can see that the largest volumes are achieved for low-repetition rate measurements (in the order of 1–10 Hz). The specific experiment of Kühn et al. (2011) represents the largest tomographic study so far achieved in an enclosure. It was conducted with helium-filled soap bubbles in an enclosure which simplifies the issue of the tracers production rate for wind tunnel experiments. From the synthetic diagram of Fig. 1, kilohertz measurements are limited to below  $100 \text{ cm}^3$  and experiments approaching 10 kHz do not exceed  $10 \text{ cm}^3$ . This is justified by the inverse proportionality between laser repetition rate and pulse energy. The extension to measurement volumes in the order of the litre cannot be envisaged for high-speed tomographic PIV systems when based on the current technology.

A possible solution is the use of larger tracer particles; however, the high relaxation time of large liquid droplets

**Fig. 1** Measurement volume versus acquisition frequency for relevant Tomographic PIV experiments in airflows. 1 Elsinga et al. (2006), 2 Humble et al. (2009), 3 Atkinson et al. (2011), 4 Schröder et al. (2011), 5 Staack et al. (2010), 6 Fukuchi (2012), 7 Kühn et al. (2011), 8 Pröbsting et al. (2013), 9 Violato et al. (2011), 10 Ghaemi and Scarano (2011), 11 Schröder et al. (2009), 12 Michaelis et al. (2012), 13 current study



poses a severe limitation to this approach. Instead, when the particle tracers have a density approaching that of the working fluid, the tracing fidelity can be maintained at larger tracer sizes (Melling 1997). For air flows, neutrally buoyant particles can be obtained by helium-filled soap bubbles (HFSB). A brief survey on the use of HFSB is given here covering some pertinent studies.

The use of HFSB as flow tracers dates back to the visualization experiments of several aerodynamic flows such as the flow around a parachute (Pounder 1956; Klimas 1973), the separated flow around an airfoil (Hale et al. 1971a), wing-tip vortices (Hale et al. 1971b) and jet flows (Ferrell et al. 1985). At low concentration, the use of HFSB is suited to visualize individual pathlines within complex flows. Although visualizations using HFSB were extended to transonic regime, where the bubbles have been observed to persist up to Mach 0.9 (Iwan et al. 1973), most applications were limited to qualitative visualization due to the uncertainty in their aerodynamic performance.

The uncertainty of measurement using helium-filled soap bubbles has been thoroughly investigated by Kerho and Bragg (1994) at the stagnation region of an airfoil with a chord of 0.5 m at free-stream velocity of 18 m/s. A commercial bubble generator producing HFSB with diameter in the range from 1 to 5 mm was used. The experiments reported a deviation of the HFSB trajectories from the theoretical streamlines due to non-neutral buoyancy of the tracers. This was mostly due to the use of a cyclone device used to reject heavier-than-air bubbles. As a result, the average population of the tracers was biased towards lighter-than-air bubbles. The authors concluded that “the use of bubbles generated by the commercially available system to trace flow patterns should be limited to qualitative measurements unless care is taken to ensure neutral buoyancy”. For this reason, the HFSB have been quantitatively used mostly in measurements of convective flows at low velocities (typically <1 m/s). Müller et al. (2000) conducted planar PIV measurement over a field-of-view of  $2 \times 2.5 \text{ m}^2$  inside an aircraft cabin using HFSB of approximately 2 mm in diameter. Müller et al. (2001) used the particle streak-tracking approach to obtain three velocity components in a plane using 1- to 2-mm-sized bubbles. A volumetric particle streak velocimetry method was used by Sun et al. (2005) in large-scale flow measurements within an aircraft cabin mock-up. Lobutova et al. (2009) adopted a 3D PTV system to characterize a Rayleigh–Bénard flow in  $130 \text{ m}^3$  using HFSB with a diameter of 4 mm. Using a bubble generator developed at the German Aerospace Centre (DLR) able to produce HFSB with typical diameter between 0.2 and 0.3 mm, Bosbach et al. (2009) conducted a large-scale planar PIV experiment with a field-of-view up to  $7 \text{ m}^2$  to investigate the convective flow within full-scale aircraft cabin. More recently, Kühn et al. (2011) assessed the feasibility

of using HFSB for large-scale tomo-PIV measurements of the flow field in a convection cell of  $75 \times 45 \times 16.5 \text{ cm}^3$ . These studies demonstrate the feasibility of conducting large-scale tomo-PIV measurements with HFSB. However, no PIV measurement has been conducted in a wind tunnel using HFSB as flow tracer. The main reason is the low seeding production rate typically achieved with bubble generators [usually below 1,000 bubbles/s (<http://www.sageaction.com/>)], which yields insufficient tracers concentration for most aerodynamic investigations.

Qureshi et al. (2007) studied the behaviour of the HFSB in nearly isotropic turbulent flow via 1D Lagrangian acoustic Doppler velocimetry. In their investigation, bubbles of diameter between 1.5 and 6 mm were employed. The authors concluded that only the turbulent pressure fluctuations at scales larger than the particles size contribute to the transport and the dispersion of the particles. As a result, sub-millimetre bubbles are required for tracing the flow when flow scales of the order of the millimetre need to be measured.

The current investigation aims at characterizing the temporal response of sub-millimetre HFSB tracers within wind tunnel experiments. The evaluation is conducted in a similar way as in Kerho and Bragg (1994), measuring the bubbles velocity around the stagnation region of a cylinder. Additionally, here, the reference velocity field is not inferred with potential flow theory, but additional PIV measurements with micron-size droplets are carried out.

The second objective of the study is to discuss the feasibility of increasing the tracer production rate to meet the requirements for the quantitative measurement of the instantaneous velocity and vorticity field in a three-dimensional volume by tomographic PIV. An experiment is conducted that illustrates the feasibility of using HFSB for time-resolved tomographic PIV in measurement domain of several litres.

## 2 Experimental apparatus and procedure

### 2.1 Wind tunnel and model

Experiments are conducted in a low-speed open-section wind tunnel (W-Tunnel) of the Aerodynamic Laboratories of the Aerospace Engineering Department at TU Delft. A 1.4-m-long rectangular channel follows the contraction nozzle. The exit cross section is  $0.4 \times 0.4 \text{ m}^2$ . A circular cylinder of 25 mm diameter is placed at the exit. This geometry is chosen for the ease of reproducibility and the scaling of the potential flow with the diameter on the front side. Moreover, the flow behaviour is stationary and the topology of the stagnation is similar to that at the leading edge of airfoils as used by Kerho and Bragg (1994). The

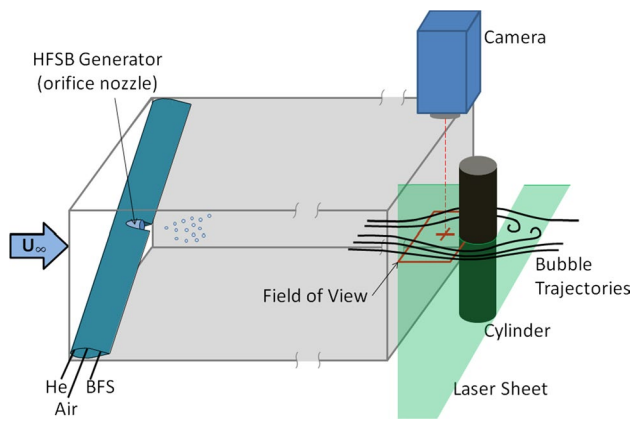


**Fig. 2** Schematic arrangement of the experiment: wind tunnel channel and exit; HFSB injection; cylinder model; illumination, imaging and measurement region

schematic layout of the experiment is illustrated in Fig. 2. Experiments are conducted at free-stream velocity of 30 m/s.

### 2.2 HFSB tracers

The HFSB generator was developed at DLR and used for several large-scale PIV experiments in buoyant flow (Bosbach et al. 2009; Kühn et al. 2011). A brief description is given here; for further details, the reader is referred to Bosbach et al. (2009). The working principle of bubble generation is based on coaxial channels terminating with a small circular orifice. The HFSB generator is fed by constant flow rates of helium, bubble fluid solution (BFS) and air. The BFS is a mixture of water, glycerine and soap. Stable operational conditions were achieved by controlling the BFS, air and helium flow using digital thermal mass-flow controllers (Bronkhorst High-Tech). Most experiments are conducted at a flow rate of 70 l/h for the air flow. Soap and helium flow rates were varied as reported in Table 1.

Given the size of the tracers and the operating flow velocity, the Reynolds number related to the bubble diameter has an order of magnitude above 10. For micron-sized tracers, the operating Reynolds is typically below unity, indicating that the interactions with the surrounding fluid pertain to the Stokes regime. Therefore, the behaviour of the tracers can be reduced to a time constant  $T$ , referred to as the relaxation time. For small, heavy particles the

relaxation time depends upon the square of the diameter and the difference in density to the fluid (Melling 1997).

Although a relaxation time for helium-filled soap bubbles  $T_{\text{HFSB}}$  may not be a constant property, dimensional considerations enable to determine its order of magnitude as the ratio between the slip velocity (i.e. the local difference between the tracer velocity  $U_{\text{HFSB}}$  and the immediately surrounding fluid velocity  $U_{\text{air}}$ ) and the local fluid parcel acceleration  $a$ .

The latter reads as

$$a = \frac{\partial U}{\partial t} + U \cdot \nabla U$$

For steady flow conditions ( $\partial U / \partial t = 0$ ), the local fluid acceleration only depends upon the transport term  $U \cdot (\nabla U)$ , which simplifies the evaluation of flow and particles acceleration from experiments. In conclusion, the estimation of the time response is evaluated according to the following expression

$$T_{\text{HFSB}} = \left| \frac{U_{\text{HFSB}} - U_{\text{air}}}{U \cdot \nabla U} \right|$$

In the present experiments, only the streamwise component is considered along the stagnating streamline.

### 2.3 Velocity measurements

The reference velocity field is obtained by PIV measurements using micron-sized droplets from a smoke generator (SAFEX *Twin Fog*). Illumination is provided by a Quantronix *Darwin-Duo* Nd:YLF, which has a nominal pulse energy of 25 mJ at 1 kHz. The beam is shaped into a light sheet of 2 mm thickness. The imaging system consists of a Photron Fast CAM SA1 camera (CMOS, 1,024 × 1,024 pixels, 12-bit, pixel pitch 20 μm). The camera is equipped with a 105-mm Nikkor objective at aperture setting of f/5.6; the imaging magnification is  $M = 0.54$ . The active size of the sensor is 608 × 448 pixels. Sequences of 5,000 double-frame images were acquired with time separation of  $\Delta t = 25 \mu\text{s}$  (for a free-stream velocity of 30 m/s) at acquisition frequency of 500 Hz. The image cross-correlation process is carried out within LaVision Davis 8.1.4 with final window size of 32 × 32 pixels and overlap factor of 75 %. The resulting vector pitch is approximately 0.3 mm.

The same equipment is used to measure the average velocity field of the HFSB tracers. Due to the much lower concentration of the HFSB tracers in the individual images,

**Table 1** Volume flow rates for HFSB production during experiments

$\dot{v}_{\text{BFS}}$ (ml/h)	3	4	5	6	3	4	5	6
$\dot{v}_{\text{He}}$ (l/h)	4	4	4	4	5	5	5	5

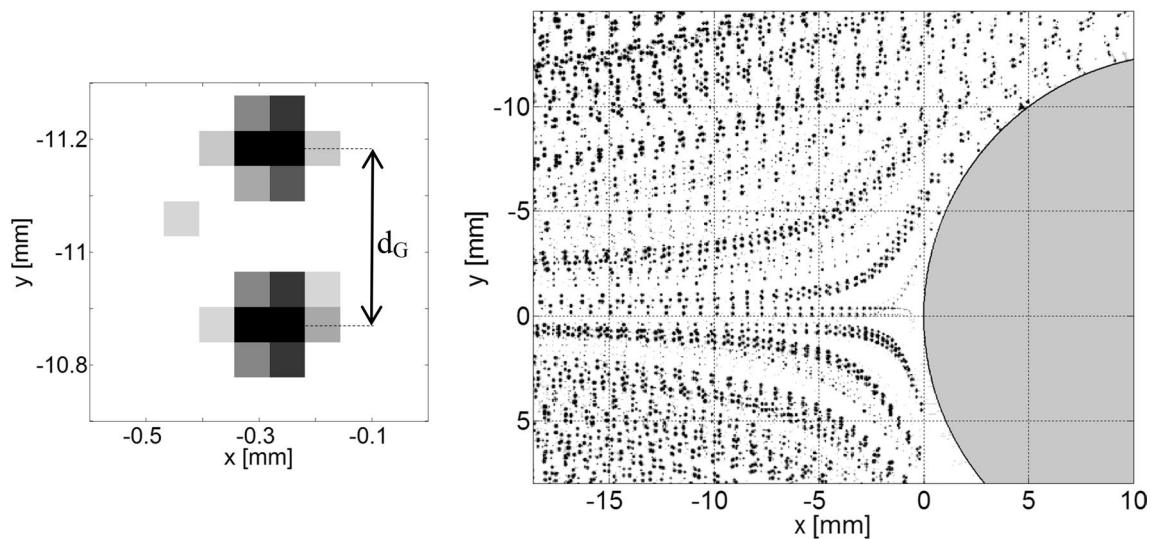


**Fig. 3** Left glare points from a single image of HFSB. Right superimposed exposures of HFSB tracers

the cross-correlation analysis is applied to a single image pair that superimposes 5,000 recordings from a sequence.

Furthermore, high-speed measurements at a rate of 20 kHz enable the analysis of the trajectory from individual HFSB tracers by the PTV technique. The analysis is made with a MATLAB script based on particle peak detection and trajectory evaluation using a velocity predictor from the fog droplet velocity field. The multi-point trajectory is regularized with a least-squares regression of a third-order polynomial based on a kernel of seven exposures. It is worth noting that every bubble produces a pair of intensity peaks, known as glare spots (van de Hulst and Wang 1991). In the present experiment, these are oriented along the vertical direction, as it is shown in Fig. 3-left. In general, the glare points are always symmetrical with respect to the bubble centre; hence, no bias error is produced in the location of the bubbles.

The glare spots are due to the first and second reflection of laser light on the outer and inner bubble surface, respectively. In the present experiment, illumination and imaging directions are approximately perpendicular. Therefore, the distance between the glare points  $d_G$  determines the bubble diameter  $d_B \approx \sqrt{2} \times d_G$ . Based on the latter hypothesis, the bubble diameter in the present experiment is estimated as  $d_B = 400 \mu\text{m}$ . The presence of the glare points poses an additional problem for the cross-correlation analysis, as the correlation map exhibits two side-peaks corresponding to the autocorrelation of the glare points. This is taken into account by ignoring the regions of the correlation map affected by the autocorrelation of the glare points. Similarly, the PTV analysis is made with the additional condition that no confusion is made in pairing the lower glare point with the higher one between subsequent exposures.

The tracking of particles is refined with sub-pixel precision using a Gaussian peak fit as commonly done in PIV. Finally, the centre of the bubble is assumed to be in the middle position between the two glare points.

#### 2.4 Aerodynamic behaviour of HFSB

The analysis of the aerodynamic behaviour of the HFSB tracers aims at determining the characteristic time scale of the tracer response. Experiments are conducted with a free-stream velocity of 30 m/s varying the soap fluid and the helium flow rate (Table 1).

The time-averaged streamlines of the HFSB are compared with the result obtained with fog droplets in Fig. 4. At the lowest helium flow rate, the streamlines of the bubbles produced with the highest soap fluid flow rate show a delayed response with respect to the decelerating air flow. Such behaviour is representative of heavier-than-air tracers. This is clearly visible from the trajectory close to the stagnation point, where the heavier tracers advance further before deviating upwards. This effect is consistently observed for all streamlines related to the condition ( $\dot{v}_{He} = 4 \text{ l/h}$ ,  $\dot{v}_{BFS} = 6 \text{ ml/h}$ ). When the rate of soap fluid is decreased, the overall density of the tracers is reduced and the deviation from the air flow trajectories becomes less significant. For  $\dot{v}_{BFS} = 4$  or  $5 \text{ ml/h}$ , the difference between air and HFSB trajectories can barely be noticed. Further reduction in the soap fluid flow produces lighter-than-air tracers, which exhibit a *floating* behaviour with respect to the pressure gradient imposed by the cylinder at stagnation. As a result, the trajectories for  $\dot{v}_{BFS} = 3 \text{ ml/h}$  depart from the air flow by anticipating the deceleration and deviating earlier from the stagnation region, similar

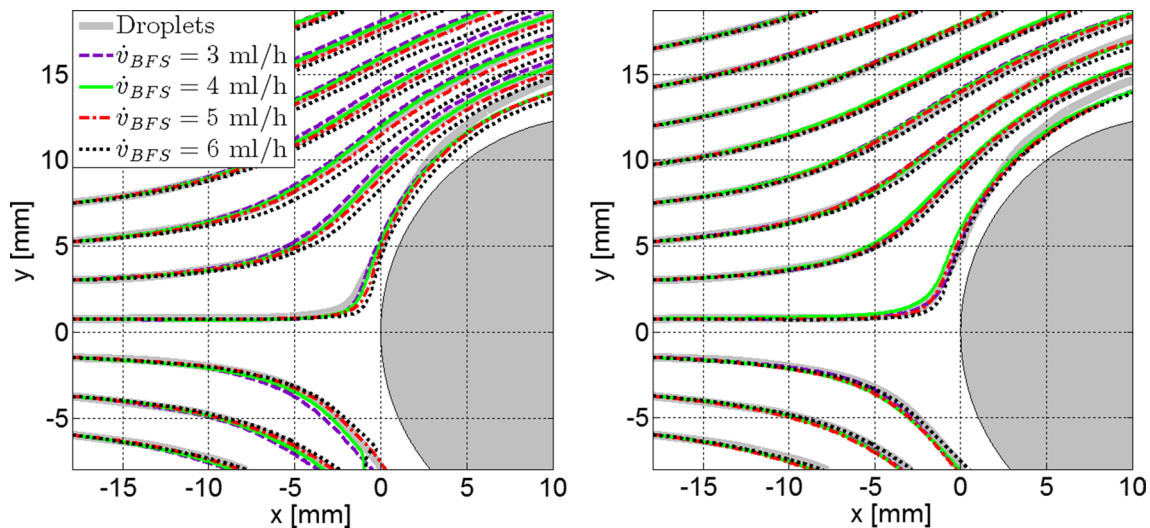
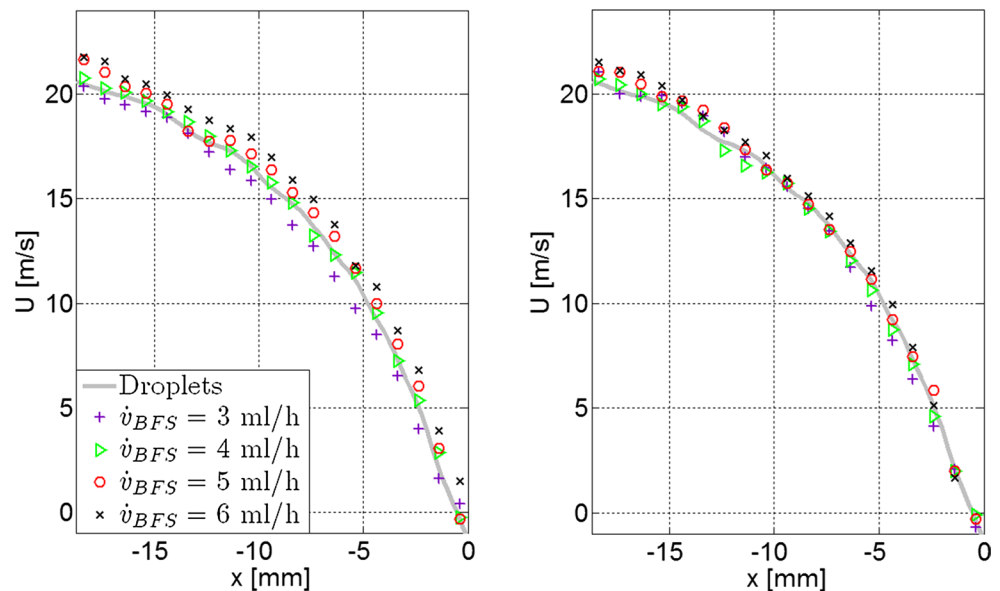


**Fig. 4** Time averaged streamlines at  $U_\infty = 30$  m/s obtained with micron-size droplets and HFSB with four different volume rates of BFS and two volume rates of helium:  $\dot{v}_{He} = 4$  l/h (left),  $\dot{v}_{He} = 5$  l/h (right). Streamlines determined by cross-correlation analysis

**Fig. 5** Comparison of HFSB velocity along the stagnation streamline. Results are shown for different values of the helium flow. Left  $\dot{v}_{He} = 4$  l/h; right  $\dot{v}_{He} = 5$  l/h



to the experiments conducted by Kerho and Bragg (1994). Results obtained at higher helium flow rate ( $\dot{v}_{He} = 5$  l/h) are included for completeness, where a similar behaviour of the tracers is noticed, although with less pronounced deviation from the air flow.

The velocity of the tracers travelling along the stagnation streamline is compared to the air flow in Fig. 5. In the range of flow rates analysed here, the maximum velocity difference is estimated around 1 m/s for the heaviest or lightest tracers. Optimal conditions are approached when  $\dot{v}_{He} = 5$  l/h and  $\dot{v}_{BFS} = 5$  ml/h. In this case, the velocity difference is estimated to be  $<0.5$  m/s. The tracing fidelity appears to be more rapidly affected by varying the

soap fluid rather than the helium flow rate. The velocity values are affected by an uncertainty of  $\pm 0.5$  m/s with a confidence level of 95 %, which was obtained using the a posteriori quantification procedure introduced by Wieneke (2014).

The velocity and acceleration of individual tracers is based on the time-resolved measurements conducted at 20 kHz. Subsequently, the *slip velocity*  $U_{BFS} - U_{air}$  between the HFSB tracers and the air flow is computed. It should be remarked that in the present case, the velocity measurements with micron droplets are considered unaffected by errors due to slip velocity. The analysis is conducted around the stagnation streamline over a stripe of approximately

**Table 2** HFSB tracing governing parameters, slip velocity, acceleration and characteristic response time for helium flow rate of  $\dot{v}_{He} = 4\text{l/h}$ 

$\dot{v}_{BFS}$ (ml/h)	Mean $U_{\text{Slip}}$ (m/s)	$a_x$ (m/s <sup>2</sup> )	$T$ ( $\mu\text{s}$ )
3	-0.37	$-1.08 \times 10^4$	31
4	-0.14	$-1.06 \times 10^4$	12
5	0.13	$-1.06 \times 10^4$	11
6	0.51	$-1.03 \times 10^4$	42

3 mm. Negative values of the mean slip velocity in Table 2 correspond to lighter-than-air bubbles with lower flow rate of BFS. Instead, a positive value of the slip velocity is associated with heavier-than-air bubbles. The standard deviation of slip velocity is computed considering the contribution of all the bubbles crossing the control volume. The mean value of the slip velocity is slightly larger than 10 cm/s, for optimal tracers, corresponding to 0.3 % of the free-stream value. This indicates that HFSB tracers in the current experiment yield a rather unbiased average velocity field.

The value of the standard deviation from tracer to tracer is comparatively larger as it attains 2 % of the free-stream velocity. This behaviour is ascribed to two possible effects. The first could be the different value of the slip velocity at varying positions in the domain. The second and more critical, following Bosbach et al. (2009), is related to the variation of bubbles properties, namely a variance in the diameter of 20 % for the same type of nozzle, in turn affecting the neutral buoyancy of HFSB.

The above measurements also yield the particles acceleration, which is reported for different values of the soap fluid flow rate (Fig. 6). The acceleration of HFSB closely follows the trend of the reference PIV data obtained with fog droplets. The lighter bubbles appear to anticipate the deceleration induced by the adverse pressure gradient emanating from the stagnation line, whereas for the heavier bubbles, the delay is not as evident.

The ratio between the local slip velocity and the acceleration returns the HFSB characteristic time response. Table 2 summarizes the results, with minimum values of  $T_{\text{HFSB}}$  in small excess of 10 microseconds. An estimate of the flow time scale for the present experiment is given by the ratio between the cylinder diameter and the velocity. For a free-stream velocity of 30 m/s,  $T_{\text{flow}} = 800 \mu\text{s}$ , which approximately two orders of magnitude above the tracers characteristic time. From the calculated values of  $T_{\text{HFSB}}$  and  $T_{\text{flow}}$ , it is concluded that in the present experiment the HFSB accurately follow the flow and can be used as flow tracers.

### 3 Tomographic PIV experiment

The HFSB tracers are used for a feasibility demonstration of time-resolved tomographic PIV within a large measurement volume in a wind tunnel. The experimental apparatus is based on that employed for the previous experiments, exception made for a number of differences discussed hereafter.

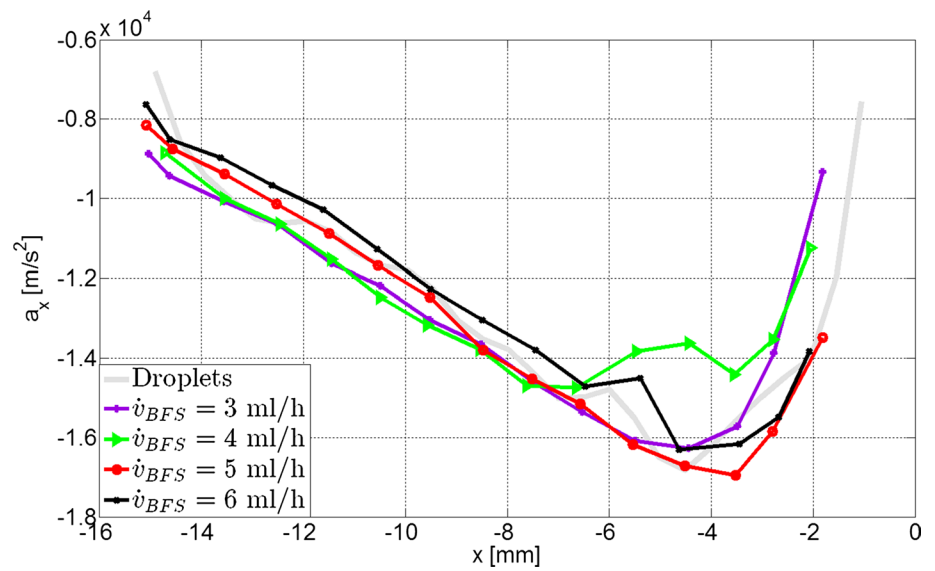
#### 3.1 Seeding system

The model is a smooth cylinder of 4.5 cm diameter, placed horizontally at the wind tunnel exit. A dedicated seeding system is realized that increases the rate of particles injected in the stream of several orders of magnitude. The system, shown in Fig. 7, is based on a piston-cylinder device. The HFSB are stored in the cylinder during production, while the piston is moved outward increasing the available volume. After a typical accumulation time of 30 s, the piston is moved rapidly inward and the air seeded with HFSB tracers is ejected. The stream with air and bubbles is transported into the settling chamber where an array of orifices distributes the tracers within a stream-tube. The latter follow the contraction along the wind tunnel nozzle resulting in a final stream-tube of approximately  $20 \times 20 \text{ cm}^2$  cross section.

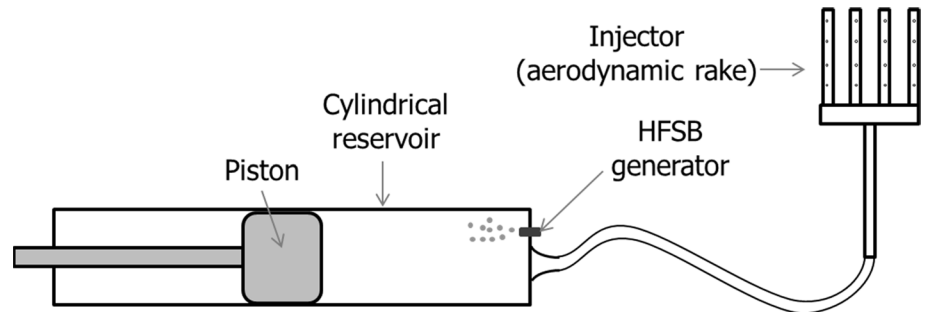
Based on particle images count, a concentration of approximately 1 particle/cm<sup>3</sup> is achieved at wind tunnel speed of 5 m/s. The laser beam is expanded to illuminate a volume of approximately 40 (length)  $\times$  12 (depth)  $\times$  20 (height) cm<sup>3</sup>. The recordings are taken at 2 kHz. Three cameras compose the tomographic imaging system. The optical magnification is approximately  $M = 0.09$ , and the extent of the observed region is  $20 \times 20 \times 12 \text{ cm}^3$  (Fig. 8). A lens aperture set to f/32 yields images in focus over the entire depth. Under these conditions, images were recorded with a particle density of approximately 0.006 ppp (6,000 particles/Mpixel) and the typical particle peak intensity was 300 counts. The background noise was approximately 10 counts. Although, large-scale tomographic PIV has been used for the evaluation of the flow structures of turbulent convective air flow in an rectangular convection cell (Kühn et al. 2011), according to a recent survey (Scarano 2013), this is the first experiment realized in a wind tunnel with time-resolved tomographic PIV over a volume of approximately 4,800 cm<sup>3</sup>.

A typical recording is shown in Fig. 9. A detail of the tracer images is displayed. Due to the low magnification factor, the glare points are imaged with a separation of 1–2 pixels. Diffraction causes the particle image diameter to exceed 2–3 pixels. As a result, no double intensity peak is observed.

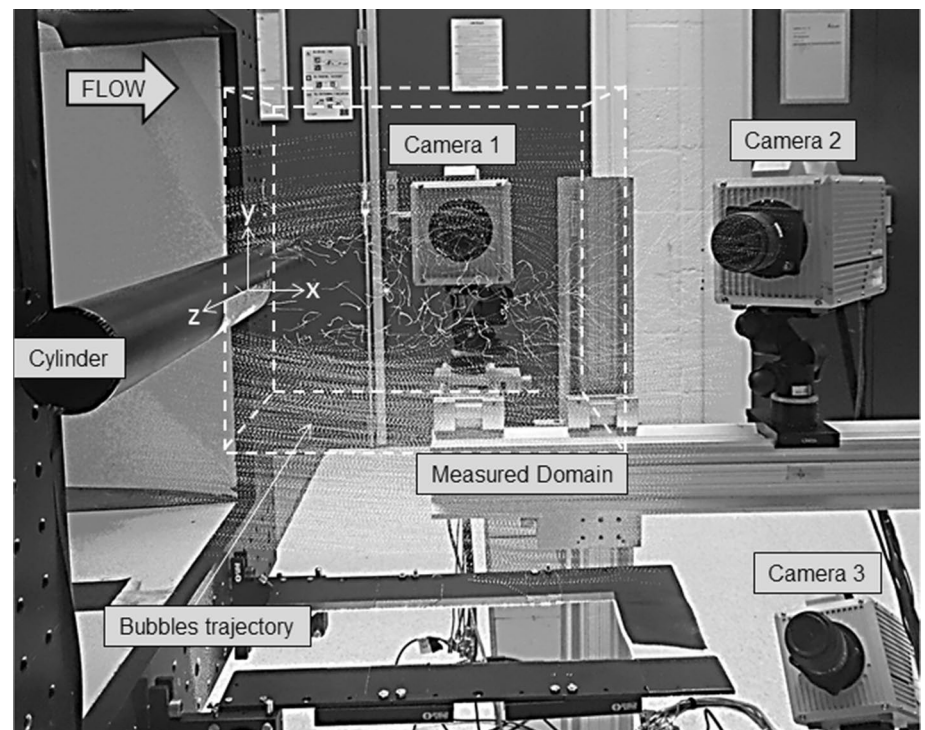
**Fig. 6** Comparison of the horizontal acceleration of the bubbles (for different BFS flow rates and  $\dot{v}_{He} = 4\text{l/h}$ ), with the time-averaged acceleration of the reference PIV data (micron-size droplets)



**Fig. 7** Schematic diagram of seeding accumulation and ejection, followed by distribution in the settling chamber



**Fig. 8** Set-up of tomographic PIV system, with cylindrical model, three-camera imaging and indication of measured domain



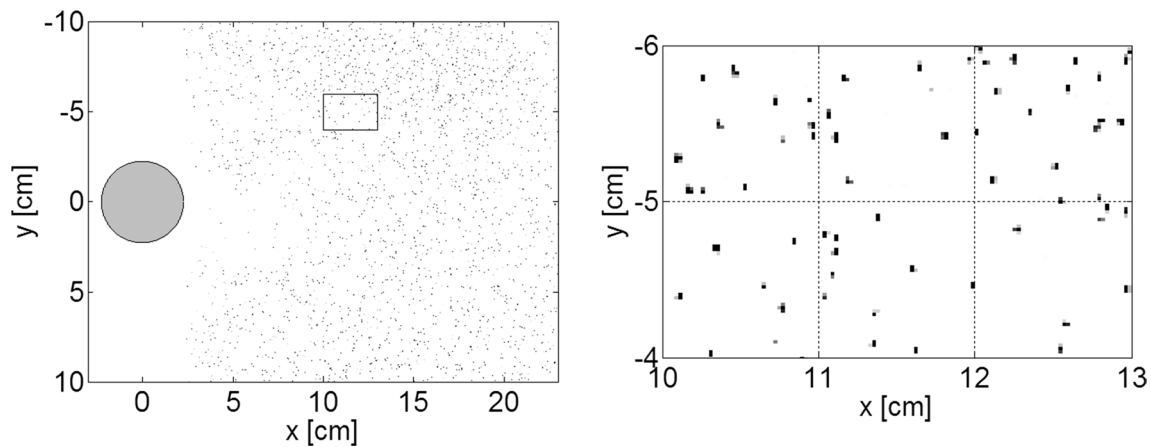
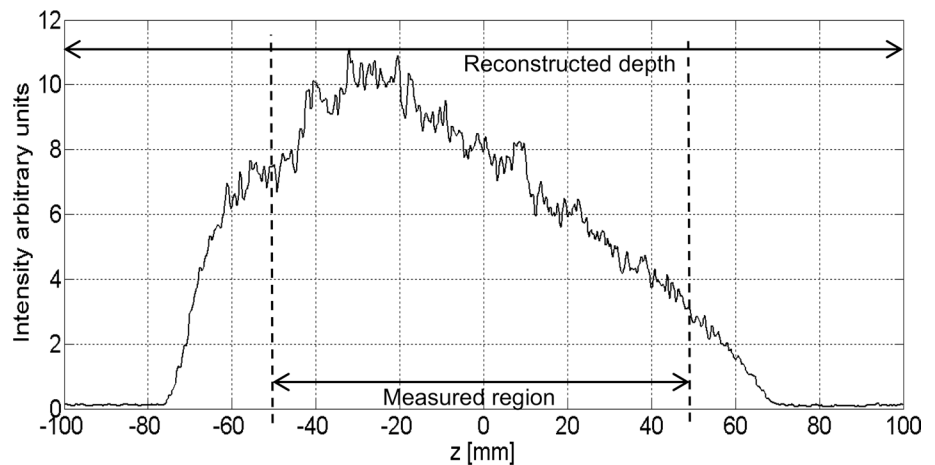


**Fig. 9** Left raw image from camera 1 (intensity with inverted colours). Right detail of particle images

**Fig. 10** Spanwise profile of reconstructed intensity light. Dashed lines indicate depth of the measured volume



The illumination distribution along the volume depth is given by the reconstructed light intensity. Integrating the intensity over 300 objects, one obtains the result shown in Fig. 10. Each point of the profile is obtained summing up values belonging to the entire plane of voxels at the same  $z$ -coordinate. The ratio of intensity inside and outside the illuminated region is indicative of the reconstruction signal-to-noise ratio  $SNR_R$ . For the present experiment  $SNR_R = 60$ . Based on a recent experimental characterization of tomographic reconstruction accuracy (Lynch and Scarano 2014), such level of  $SNR_R$  implies that the ghost particles velocity does not affect the velocity estimates from cross-correlation (Elsinga et al. 2006).

### 3.2 Instantaneous velocity field

The tomographic data analysis is performed with LaVision software Davis 8.2. Before volume reconstruction, standard image pre-processing for tomo-PIV is conducted, which consists of image background elimination via

minimum subtraction and Gaussian filter to regularize the particle image intensity distribution. The domain is discretized into  $1,000 \times 1,000 \times 500$  voxels and reconstructed with the MART algorithm using the fast MART approach. The objects are interrogated with correlation blocks of  $96 \times 96 \times 86$  voxels ( $2.1 \times 2.1 \times 1.9 \text{ cm}^3$ ) and 75 % overlap factor, with a sparse direct correlation algorithm (Discetti and Astarita 2012), yielding a measurement of  $50 \times 50 \times 24$  vectors with a grid spacing of 5 mm.

The resulting vector field is post-processed with the universal outlier detection (Westerweel and Scarano 2005) and filtered with a second-order polynomial in the time domain with a kernel of seven snapshots. Figure 11 illustrates the results in terms of velocity vectors and  $z$ -vorticity contours at the plane corresponding to  $z = 0$ . The sequence illustrates the spatio-temporal development of the *Kármán Street* composed of counter-rotating vortices shedding from the rear side of the cylinder. The limited spatial resolution, mostly due to the sparse seeding, does not allow resolving the thin shear layer prior to the vortex roll-up, as well

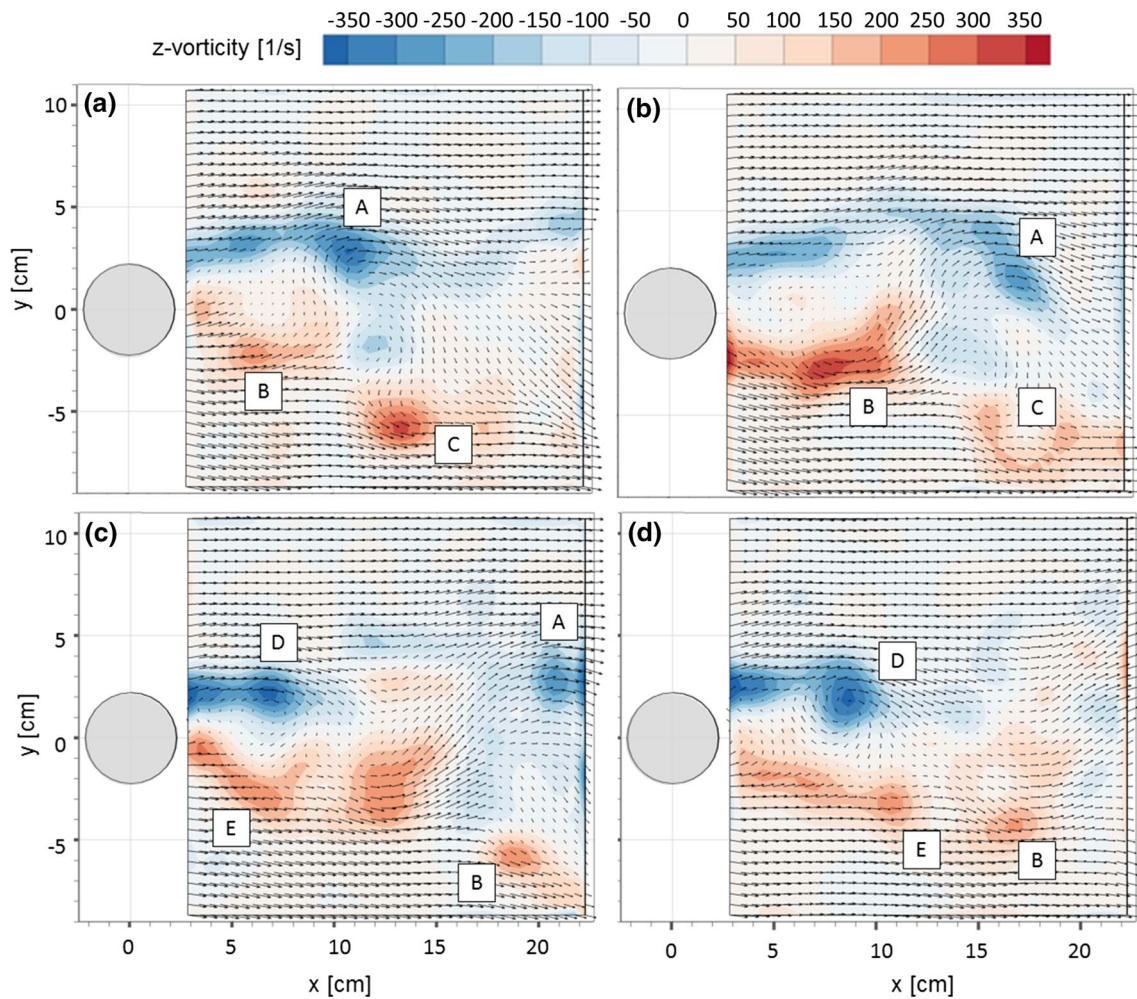


**Fig. 11** Spanwise vorticity contour at four time instants: **a**  $t = 0$  ms, **b**  $t = 15$  ms, **c**  $t = 30$  ms, **d**  $t = 45$  ms (shedding period:  $T = 60$  ms)

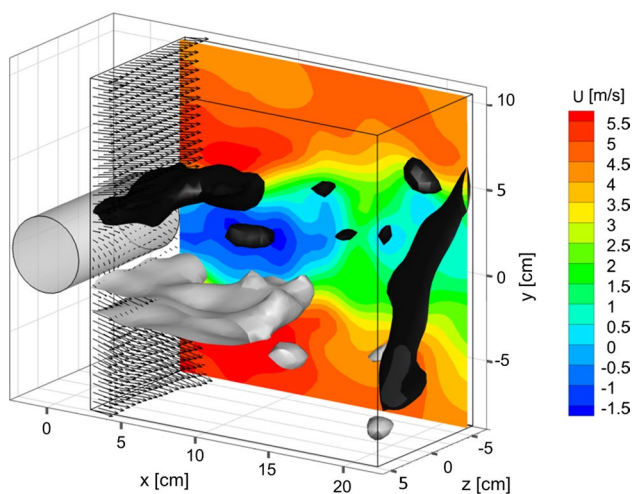


**Fig. 12** Instantaneous velocity and vorticity distribution in the wake of the cylinder. Dark and light grey iso-surfaces correspond to spanwise vorticity of  $\pm 300$  1/s, respectively

as the turbulent sub-structures such as the *ribs* or *fingers* reported in previous tomographic experiments on the same geometry (Elsinga et al. 2006; Scarano and Poelma 2009). In the three-dimensional snapshot represented in Fig. 12, the iso-surface of vorticity magnitude reveals both shear layers developing from the cylinder surface. The cross-correlation signal-to-noise ratio (Keane and Adrian 1992) typically exceeds 2.5 in the outer region, while it drops to 1.4 in the near wake region as a result of the lower tracer concentration.

#### 4 Conclusions

The tracing fidelity of sub-millimetre HFSB tracers is investigated with experiments conducted in an aerodynamic wind tunnel. The stagnation region in front of a circular cylinder provides a steady and inviscid flow region

to evaluate accurately flow velocity, acceleration and tracers slip velocity. The analysis covers varying values of the mass flow rate of the bubble components, leading to an optimum condition that corresponds to minimum slip velocity. The estimated characteristic response time scale is in the range of 10  $\mu\text{s}$ , which demonstrates the applicability of HFSB tracers for quantitative velocimetry in wind tunnel flows. The present result is in contrast to the earlier study conducted by Kerho and Bragg (1994). The main difference to the latter work is the significantly smaller size of the tracers (300 microns versus several millimetres) and no need of pre-filtering of negatively buoyant particles.

Time-resolved tomographic PIV experiments on a large volume required a specialized seeding system to temporarily increase the number of tracers in the flow. A seeding accumulator and transient injector could yield a particle concentration of approximately 1 particle/cm<sup>3</sup> in a volume of approximately 4,800 cm<sup>3</sup>. Tomographic PIV analysis could be performed with spatial cross-correlation, yielding the instantaneous large-scale flow structures in the wake of a cylinder. The level of spatial resolution is mostly restricted by the low concentration of tracers. Further developments aim at increasing the HFSB production rate, as well as their confinement within a selected stream tube using local injection.

**Open Access** This article is distributed under the terms of the Creative Commons Attribution License which permits any use, distribution, and reproduction in any medium, provided the original author(s) and the source are credited.

## References

- Adrian RJ (2005) Twenty years of particle image velocimetry. *Exp Fluids* 39:159–169
- Atkinson C, Coudert S, Foucaut JM, Stanislas M, Soria J (2011) The accuracy of tomographic particle image velocimetry for measurements of a turbulent boundary layer. *Exp Fluids* 50:1031–1056
- Beaudoin JF, Aider JL (2008) Drag and lift reduction of a 3D bluff body using flaps. *Exp Fluids* 44:491–501
- Bosbach J, Kühn M, Wagner C (2009) Large scale particle image velocimetry with helium filled soap bubbles. *Exp Fluids* 46:539–547
- Carmer CF, Konrath R, Schroder A, Monnier JC (2008) Identification of vortex pairs in aircraft wakes from sectional velocity data. *Exp Fluids* 44:367–380
- Discetti S, Astarita T (2012) Fast 3D PIV with direct sparse cross-correlations. *Exp Fluids* 53:1437–1451
- Elsinga GE, Scarano F, Wieneke B, Van Oudheusden BW (2006) Tomographic particle image velocimetry. *Exp Fluids* 41:933–947
- Ferrell GB, Aoki K, Lilley DG (1985) Flow visualization of lateral jet injection into swirling crossflow. *AIAA Paper 85(0059)*:14–17
- Fukuchi Y (2012) Influence of number of cameras and preprocessing for thick volume tomographic PIV, 16th international symposium on applications of laser techniques to fluid mechanics, (Lisbon, Portugal)
- Ghaemi S, Scarano F (2010) Multi-pass light amplification for tomographic particle image velocimetry application. *Meas Sci Technol* 21:127002
- Ghaemi S, Scarano F (2011) Counter-hairpin vortices in the turbulent wake of a sharp trailing edge. *J Fluid Mech* 689:317–356
- Hale RW, Tan P, Ordway DE (1971a) Experimental investigation of several neutrally-buoyant bubble generators for aerodynamic flow visualization. *Nav Res Rev* 24:19–24
- Hale RW, Tan P, Stowell RC, Ordway DE (1971b) Development of an integrated system for flow visualization in air using neutrally-buoyant bubbles, SAI-RR 7107, SAGE ACTION Inc. Ithaca, NY
- Humble RA, Elsinga GE, Scarano F, Van Oudheusden BW (2009) Three-dimensional instantaneous structure of a shock wave/turbulent boundary layer interaction. *J Fluid Mech* 622:33–62
- Iwan LS, Hale RW, Tan P, Stowell RC (1973) Transonic flow visualization with neutrally-buoyant bubbles, SAI-RR 7304. Ithaca, NY
- Keane RD, Adrian RJ (1992) Theory of cross-correlation analysis of PIV images. *Appl Sci Res* 49:191–215
- Kerho MF, Bragg MB (1994) Neutrally buoyant bubbles used as flow tracers in air. *Exp Fluids* 16:393–400
- Klimas P (1973) Helium bubble survey of an opening parachute flow-field. *J Aircraft* 10:567–5694
- Kompenhans J, Raffel M, Dieterle L, Dewhirst T, Vollmers H, Ehrenfried K, Willert C, Pengel K, Kähler C, Schröder A, Ronneberger O (2000) Particle image velocimetry in aerodynamics: Technology and applications in wind tunnels. *J Visual* 2:229–244
- Kühn M, Ehrenfried K, Bosbach J, Wagner C (2011) Large-scale tomographic particle image velocimetry using helium-filled soap bubbles. *Exp Fluids* 50:929–948
- Lignarolo LEM, Ragni D, Krishnaswami C, Chen Q, Simão Ferreira CJ, Van Bussel GJW (2014) Experimental analysis of the wake of a horizontal-axis wind-turbine model. *Renew Energy* 70:31–46
- Lobutova E, Resagk C, Rank R and Müller D (2009) Extended three dimensional particle tracking velocimetry for large enclosures. In *Imaging measurement methods for flow analysis* (pp. 113–124). Springer, Berlin
- Lynch KP, Scarano F (2014) Experimental determination of tomographic PIV accuracy by a 12-camera system. *Meas Sci Technol* 25:084003
- Melling A (1997) Tracer particles and seeding for particle image velocimetry. *Meas Sci Technol* 8:1406
- Michaelis D, Bomphrey R, Henningsson P, Hollis D (2012) Reconstructing the vortex skeleton of the desert locust using phase averaged POD approximations from time resolved thin volume tomographic PIV, 16th international symposium on applications of laser techniques to fluid mechanics, (Lisbon, Portugal)
- Müller RHG, Flögel H, Scherer T, Schaumann O, Markwart M (2000) Investigation of large scale low speed air conditioning flow using PIV, 9th international symposium on flow visualization, (Edinburgh, UK)
- Müller D, Müller B, Renz U (2001) Three-dimensional particle-streak tracking (PST) velocity measurements of a heat exchanger inlet flow. *Exp Fluids* 30:645–656
- Pounder E (1956) Parachute inflation process Wind-Tunnel Study, WADC Technical report 56-391, Equipment Laboratory, Wright-Patterson Air Force Base. Ohio, USA, pp 17–18
- Pröbsting S, Scarano F, Bernardini M, Pirozzoli S (2013) On the estimation of wall pressure coherence using time-resolved tomographic PIV. *Exp Fluids* 54:1–15
- Qureshi NM, Bourgoin M, Baudet C, Cartellier A, Gagne Y (2007) Turbulent transport of material particles: an experimental study of finite size effects. *Phys Rev Lett* 99(18):184502-1–184502-4
- Raffel M, Willert CE, Wereley ST, Kompenhans J (2007) *Particle Image Velocimetry -A Practical Guide*, 2nd edn. Springer, Berlin Heidelberg
- Scarano F (2013) Tomographic PIV: principles and practice. *Meas Sci Technol* 24:012001
- Scarano F, Poelma C (2009) Three-dimensional vorticity patterns of cylinder wakes. *Exp Fluids* 47:69–83

- Schröder A, Geisler R, Elsinga GE, Scarano F, Dierksheide U (2008) Investigation of a turbulent spot and a tripped turbulent boundary layer flow using time-resolved tomographic PIV. *Exp Fluids* 44:305–316
- Schröder A, Geisler R, Sieverling A, Wieneke B, Henning A, Scarano F, Elsinga GE, Poelma C (2009) Lagrangian aspects of coherent structures in a turbulent boundary layer flow using TR-Tomo PIV and FTV, 8th international symposium on particle image velocimetry, (Melbourne, Victoria, Australia)
- Schröder A, Geisler R, Staack K, Elsinga GE, Scarano F, Wieneke B, Westerweel J (2011) Eulerian and Lagrangian views of a turbulent boundary layer flow using time-resolved tomographic PIV. *Exp Fluids* 50:1071–1091
- Staack K, Geisler R, Schröder A, Michaelis D (2010) 3D-3C-coherent structure measurements in a free turbulent jet, 15th international symposium on applications of laser techniques to fluid mechanics, (Lisbon, Portugal)
- Sun Y, Zhang Y, Wang A, Topmiller JL and Bennet JS (2005), Experimental characterization of airflows in aircraft cabins, Part I: experimental system and measurement procedure, ASHRAE transactions 111
- Van de Hulst HC, Wang RT (1991) Glare points. *Appl Optics* 30:4755–4763
- Violato D, Moore P, Scarano F (2011) Lagrangian and Eulerian pressure field evaluation of rod-airfoil flow from time-resolved tomographic PIV. *Exp Fluids* 50:1057–1070
- Westerweel J, Scarano F (2005) Universal outlier detection for PIV data. *Exp Fluids* 39:1096–1100
- Westerweel J, Elsinga GE, Adrian RJ (2013) Particle image velocimetry for complex and turbulent flows. *Annu Rev Fluid Mech* 45:409–436
- Wieneke B (2014) Generic a posteriori uncertainty quantification for PIV vector fields by correlation statistics, 17th international symposium on applications of laser techniques to fluid mechanics (Lisbon, Portugal)